Technology

Molecular Cell

The Oscillating Stimulus Transporter Assay, OSTA: Quantitative Functional Imaging of Transporter Protein Activity in Time and Frequency Domains

Graphical Abstract

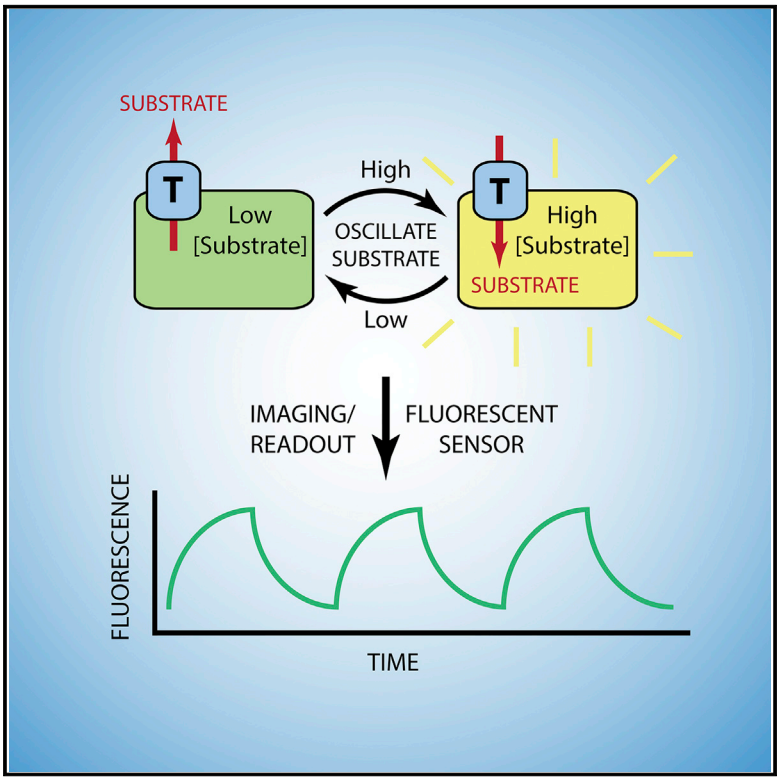

Authors

Jacob P. Keller, Loren L. Looger

Correspondence

jacobpkeller@gmail.com (J.P.K.),
loogerl@janelia.hhmi.org (L.L.L.)

In Brief

Functional assays of transporter proteins have typically been cumbersome and imprecise. Keller and Looger introduce an easy-to-implement assay that provides high-precision quantitative temporal readouts of transporter activity through the use of oscillating stimuli, biosensors, and functional imaging.

Highlights

- Provides individual temporal readouts of transporter function from hundreds of cells
- Uses commonly available lab apparatus: fluorescence microscope and perfusion system
- Oscillating responses can be used to find cells, potentially to quantify function
- Applicable to wide range of transporters, potentially high-throughput drug screening

Keller & Looger, 2016, Molecular Cell *64*, 199–212
October 6, 2016
http://dx.doi.org/10.1016/j.molcel.2016.09.001

CellPress

Molecular Cell
Technology

The Oscillating Stimulus Transporter Assay, OSTA: Quantitative Functional Imaging of Transporter Protein Activity in Time and Frequency Domains

Jacob P. Keller[1,2,*] and Loren L. Looger[1,*]
[1]Janelia Research Campus, Howard Hughes Medical Institute, Ashburn, VA 20147, USA
[2]Lead Contact
*Correspondence: jacobpkeller@gmail.com (J.P.K.), loogerl@janelia.hhmi.org (L.L.L.)
http://dx.doi.org/10.1016/j.molcel.2016.09.001

SUMMARY

Transmembrane transporter proteins allow the passage of essentially all biologically important molecules across the lipid membranes of cells and organelles and are therefore of central importance to all forms of life. Current methods of transporter measurement, however, are lacking in several dimensions. Herein, a method is presented in which oscillating stimuli are presented to transporter-expressing cells, and activity is measured through imaging the corresponding oscillating responses of intracellular fluorescent sensors. This approach yields continuous temporal readouts of transporter activity and can therefore be used to measure time-dependent responses to drugs and other stimuli. Because of the periodic nature of the response, temporal Fourier transforms can be used to identify and quantify regions of interest in the xy plane and to overcome noise. This technique, called the Oscillating Stimulus Transporter Assay (OSTA), should greatly facilitate both functional characterization of transporters as well as high-throughput screening of drugs for transporters of particular pathophysiological interest.

INTRODUCTION

Transmembrane transporter proteins enable the passage of nearly all biologically relevant molecules across the otherwise-impermeable lipid membranes of cells and organelles and, as such, are of great importance to life. They constitute > 10% of the human proteome, and mutations thereof are implicated in a wide range of human genetic diseases and cancers (Sahoo et al., 2014). Despite this importance, development of methods for functional measurement has been stunted. For one, since transporter proteins are embedded in lipid membranes, purification of active transporters is often difficult or impossible, dramatically hampering in vitro characterization. Furthermore, even when they can be purified, transporters must then be reconstituted in a way that allows for measurement of substrate translocation from one defined compartment to another. Although this can be done in a number of ways, such as in liposomes (Scalise et al., 2013) or nanodevices (Watanabe et al., 2014), it nevertheless remains a significant obstacle. In the majority of cases, these obstacles can be circumvented altogether by measuring activity of transporters in situ, in cells expressing the transporter of interest. The remaining obstacle, measurement of substrate concentrations over time, has therefore generally represented the greatest hindrance to transporter functional measurements.

One successful approach to measuring substrate passage is electrophysiology, which measures electrical currents sometimes associated with transporter activity. Electrophysiological methods are sensitive and have excellent resolution in time, as exemplified by single ion channel current measurements (Sakmann and Neher, 2009). Electrophysiology, however, remains low-throughput, laborious, and technically challenging despite recent attempts at improvements in throughput (e.g., Dunlop et al., 2008). Additionally, conventional electrophysiology cannot be used with all transporters, since transporter currents are often small or simply do not exist (in the case of non-electrogenic transporters). To address this, substrate-selective electrodes can sometimes be used (Miller, 1995; Musa-Aziz et al., 2010). These glass electrodes, filled with an analyte-responsive medium, are inserted into or apposed to cells, and currents are recorded. Unfortunately, substrate selectivity can be poor, and the range of substrates is limited. Further, throughput and laboriousness remain problematic. As such, while electrophysiology works in a subset of cases, it has a number of features that limit its applicability.

The most generally applicable and common method for transporter measurement employs radiolabels to track substrates (Clarke and Khalid, 2015). Cultured cells expressing the transporter of interest are exposed to radiolabeled substrate, and changes in cellular radioactivity are measured at set time points. The certitude afforded by changes in radioactivity, along with a long scientific history and the relative ease of procuring radioactive substrate analogs, are the main reasons for the method's popularity, and its validity remains uncontested. The drawbacks, however, are many. Working with radiolabeled materials requires dedicated equipment, and special measures must be taken both in the lab and administratively. Further, time points are sparse, readings are imprecise, and even these coarse measurements require optimization of experimental parameters. To ensure that results are robust, controls and normalizations must be

carried out to determine actual transfection efficiencies, protein amounts, etc. It is additionally necessary to separately assess membrane targeting of proteins as well as the integrity of the constituent cells. Accordingly, while there is justification for radio-isotope transporter assays based on their time-tested reliability, there are also drawbacks.

Functional fluorescence imaging (Zhang et al., 2002) is a valuable tool for cell biology, but it has not yet been used extensively for transporter measurements. Although there are historical reasons for its neglect, its limitations have largely disappeared. Previously, computer hardware and software were often insufficient for processing imaging datasets. Now, with advances in hardware and with the advent of powerful and versatile software like ImageJ (Schneider et al., 2012), sophisticated image-processing algorithms can be run on a standard computer. Similar advances have been made in microscope instrumentation, allowing for signal-to-noise ratios and temporal precision approaching that of electrophysiological techniques (Canepari and Zecevic, 2010).

The key step in functional imaging is selecting the appropriate ligand-specific sensor for imaging. There are now many small molecular fluorescent indicators with specificities for H^+/pH (SNARFs, BCECF), Ca^{2+} (Furas, OGB, Fluos, Indos), Mg^{2+} (mag-Indo, mag-Fura, mag-Fluo), and transmembrane potential (di-ANNEPSs, PeTs) (reviewed in Spence and Johnson, 2010; see also Woodford et al., 2015). Some of these can be used for the measurement of other substrates, e.g., H^+ sensors can be used to detect changes in OH^- or HCO_3^- (see data herein, for example). These dyes have been improved significantly over the years and continue to improve, in terms of photostability, control of localization, and signal (e.g., the recently developed Fluo-4XL calcium indicator has a dF/F of ~270 [L. Lavis, personal communication]). Therefore, if the transporter of interest traffics one of these substrates, dyes can be used for functional imaging.

More recently, fluorescent protein-based ("genetically encoded") indicators have blossomed, harnessing the diversity of naturally evolved proteins specific for an enormous range of molecules (for reviews, see Broussard et al., 2014; Enterina et al., 2015). Indicators for analytes of particular interest, such as Ca^{2+} (Chen et al., 2013) and glutamate (Marvin et al., 2013), have achieved sufficient signal-to-noise, kinetics, brightness, and photostability to facilitate long-term in vivo imaging (Cichon and Gan, 2015). Other notable indicators include those for voltage (Abdelfattah et al., 2016; Gong et al., 2015; Treger et al., 2015), Cl^- (Arosio and Ratto, 2014; Grimley et al., 2013), and pH (Miesenböck et al., 1998; Shen et al., 2014). Given the range of molecules recognized by naturally occurring proteins (e.g., antibodies or periplasmic binding proteins; Dwyer and Hellinga, 2004), the use of protein engineering to tailor such binding specificity (Marvin and Hellinga, 2001; Tinberg et al., 2013), and increased capability to convert proteins into genetically encoded sensors (e.g., Marvin et al., 2011), it is likely that sensors will continue to proliferate in the coming years. While ligand transport has occasionally been monitored through genetically encoded sensors, e.g., sugar flux in *Arabidopsis* (Chaudhuri et al., 2008; Fehr et al., 2005), its capabilities remain largely untapped.

Herein a combined oscillating stimulus protocol and complementary image analysis approach, which comprise the Oscillating Stimulus Transporter Assay (OSTA), are presented. Simple to implement, OSTA provides high-quality characterization of transporter function in short periods of time. Further, the use of an oscillating stimulus increases the temporal sampling density to such a degree that transporter function can be monitored as a function of time. A further advantage of the oscillating stimulus is that it evokes an oscillating response of the same frequency, the magnitude and phase of which can be used in image segmentation into regions of interest (ROIs). The method is demonstrated herein through functional measurements of a variety of transporters and sensors, with multiple substrates and control conditions. Both theoretical and practical considerations are presented to guide future experimental design. Generally, there is great potential to apply OSTA both in characterization of novel or unannotated transporter function as well as in high-throughput screening of medically relevant transporter drug targets.

DESIGN

The experimental scheme is relatively simple (Figure 1): cells expressing the transporter of interest are loaded with a small-molecule- or genetically encoded fluorescent sensor and are perfused with solutions oscillating between high and low substrate concentrations. In all cases tested, oscillation periods of 10–120 s were sufficient to provoke measureable responses with minimal optimization. This shortness of period is likely attributable to the high surface-to-volume ratio of the adherent HEK293 cells used in this study (at least one million-fold larger compared to *Xenopus* oocytes). Microscopic fields of view contained from tens to hundreds of cells from transporter-positive and transporter-negative groups. Functional readouts were extracted from time-lapse movies taken on an inverted confocal fluorescence microscope (Leica LSM-510) with frame rates of 1–2 Hz and were processed in FIJI/ImageJ (Schindelin et al., 2012; Schneider et al., 2012) according to the particulars of the experiment. This experimental design, though simple, enabled facile and rapid measurement of a wide variety of transporter properties.

RESULTS

Example 1: Slc26a3-Mediated Cl^-/HCO_3^- Exchange and Salicylate Inhibition

Slc26a3 (A3), a Cl^-/HCO_3^- exchanger, is expressed in many tissues where it plays various roles in pH regulation and chloride balance (Ohana et al., 2009). Known to interact directly with the cystic fibrosis transmembrane conductance regulator protein (CFTR), A3 likely plays a central role in cystic fibrosis (Ko et al., 2004). Further, mutations in A3 also cause congenital chloride diarrhea (Höglund et al., 1996). Since previous work had characterized the Cl^-/HCO_3^- exchange of A3 (Keller et al., 2013; Lamprecht et al., 2005, 2006, 2009; Ohana et al., 2011), it was selected as an appropriate transporter with which to test the OSTA method (Figure 2). Cells expressing A3 were loaded with the pH-sensitive dye SNARF-5F-AM and perfused with

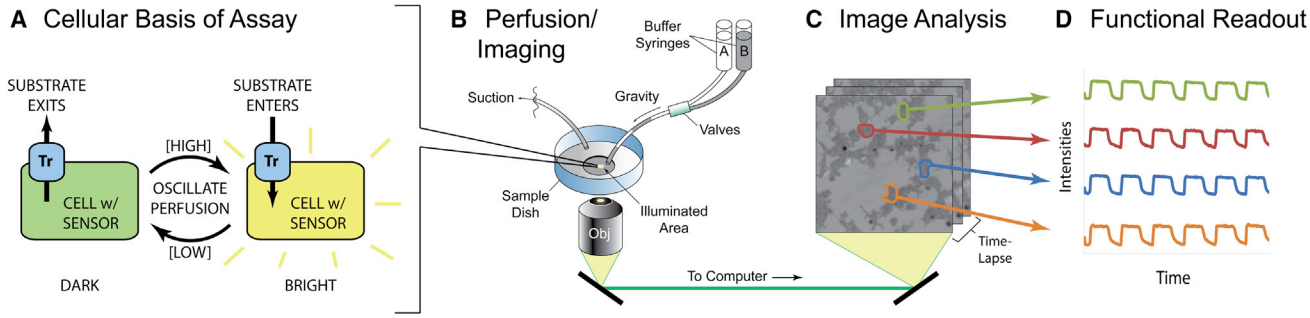

Figure 1. Schematic of Experimental Technique

(A) Concept of assay: cells expressing transporter of interest and loaded with fluorescent sensor are perfused with alternating buffers ± substrate, resulting in oscillating changes in fluorescence.

(B) Physical implementation: cells in a culture dish are imaged in an inverted fluorescence microscope while buffers are perfused onto the sample using a simple gravity-fed system switched with computer-controlled valves. Other workable variations are conceivable.

(C) Image analysis of resulting image stacks can be done in any number of ways, depending on the experiment. Typically all processing can be done in ImageJ/FIJI.

(D) After processing, traces are plotted as desired.

buffers oscillating every 5 s (total period 10 s) between 8 and 158 mM Cl^-, in the presence of 25 mM HCO_3^-, with a confocal microscope frame rate of ~2 Hz (Figure 2A). A uniform oscillating response in the SNARF-5F signal was observed to follow the stimulus in the expected manner (Figures 2B–2D). Since the drug salicylate inhibits a non-transporting paralog to A3, prestin (Slc26a5) (Santos-Sacchi et al., 2006; Zheng et al., 2000), 10 mM salicylate was added to the buffers to determine its effect on A3. At this concentration, salicylate was found to nearly completely abrogate the oscillating response, and subsequent washout showed a return to the initial oscillating response. Further studies are underway to quantify the affinity (IC_{50}) and to explore physiological implications of this interaction. Thus, in an experiment of 15 min duration, not only was the OSTA paradigm demonstrated and previous results confirmed, but a novel hypothesis was also tested and confirmed, at least on a preliminary level.

Example 2: Slc26a2-Mediated SO_4^{2-}/OH^- Exchange as a Function of Extracellular Cl^- and pH

Another transporter from the Slc26 family, Slc26a2 (A2), has been implicated in a number of osteochondrodysplasias (bone growth abnormalities) due to mutations affecting its normal SO_4^{2-}/OH^- exchange activity (Dawson and Markovich, 2005), which is critical for sulfation of cartilage and extracellular matrix. Normal transport has been reported to require extracellular Cl^- to allosterically gate the normal SO_4^{2-}/OH^- exchange function (Ohana et al., 2012). Thus, an experiment was devised in which permutations of SO_4^{2-}, Cl^-, and OH^- could be perfused onto SNARF-5F-loaded cells expressing A2 (Figure 2E). The primary stimulus was oscillation of SO_4^{2-} from 0 to 100 mM, with a period of 40 s, and this was continued throughout the entire experiment. In the first phase of the experiment (Figures 2F–2H), the buffers were held at pH 7.5 and 0 Cl^-. As expected, this resulted in negligible oscillations in transport signal due to lack of extracellular Cl^-, but when 10 mM Cl^- was superadded to these solutions, oscillations became apparent, consistent with the reported allosteric necessity of Cl^- for transport. The same regimen was repeated at pH 6.85, with greatly diminished but still marked oscillation amplitudes in the Cl^--containing condition, and at pH 8.5, which replicated the pH 7.5 condition. This lack of difference between pH 7.5 and 8.5 was unexpected, since the concentration of the transporter's reported substrate, OH^-, increases 10-fold from pH 7.5 to pH 8.5. The unexpected result can perhaps be attributed to saturation of the OH^- binding site, but was not explored further.

It was also noticed that the average "tonic" intracellular pH in the absence of extracellular chloride was always lower in A2-expressing cells than in controls. This was consistent with claims that extracellular chloride is required only for influx of OH^-, and not for efflux (Ohana et al., 2012). The transport cycle in the absence of Cl^- would thus favor efflux of OH^- and would lower intracellular pH, as observed herein. The inverse finding, however, was also observed: in the presence of extracellular chloride, tonic intracellular pH was higher in A2-expressing cells than in controls. One possible explanation is that Cl^- not only gates OH^- entry, but might also dictate asymmetry in the transport process, perhaps by allosterically biasing the transporter toward a conformation favorable to OH^- influx. Further studies, however, will be needed to confirm this possibility. In any case, this experiment demonstrates the ease with which transporter function under various permutations of conditions can be quickly yet rigorously tested by the OSTA method.

Example 3: Dapagliflozin Inhibition of the Na^+/Glucose Cotransporter Sglt2

To explore the OSTA's efficacy on transporters of more diverse types, experiments were designed to test the diabetes-related drug target Sglt2. This Na^+/glucose cotransporter is expressed physiologically in the kidney, where, driven by sodium gradients, it recovers the majority of the glucose initially filtered into the urine (Wright, 2001). Potent and specific inhibitors have been developed, with the rationale that significant amounts of glucose could be removed from the circulation by blocking recovery and allowing it to be excreted from the body in urine. Some of these inhibitors, most notably the gliflozins, are clinically approved and in use (Meng et al., 2008). Unfortunately, Sglt2 tends to have a

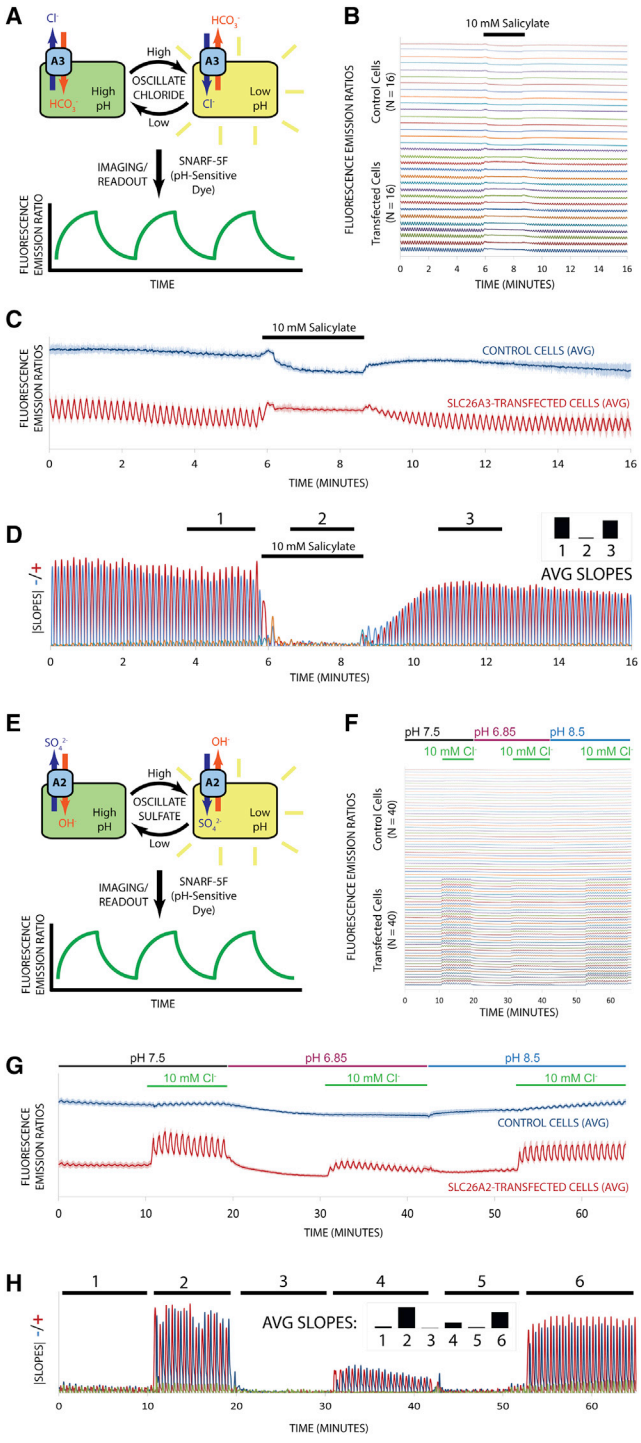

Figure 2. Slc26 Transporters: Slc26a3-Mediated Cl^-/HCO_3^- Exchange Is Inhibited by 10 mM Salicylate; Slc26a2-Mediated OH^-/SO_4^{2-} Exchange under Various Conditions

(A) Schematic: cells expressing Slc26a3 and loaded with SNARF-5F-AM ratiometric pH indicator dye were perfused with buffers oscillating between 8 and 158 mM chloride ± 10 mM sodium salicylate. Signal is the ratio between two emission bands excited with one wavelength (Ex 514 nm, Em 530–595, 600–735 nm; objective Plan-Apochromat 20×/0.8 NA, imaging rate ~2 Hz; stimulus period 10 s).

low flux rate in various expression systems (Wright, 2001) and is therefore difficult to measure in conventional transport assays. To test the measurability of Sglt2's transport under the OSTA paradigm, cells were co-transfected with both Sglt2 and a novel intracellular ratiometric fluorescent glucose sensor protein (J.P.K., A. Simon, J.S. Marvin, J. Shea, H. Lacin, W. Lemon, A. Carruthers, M. Koyama, and L.L.L., unpublished data) and subjected to oscillations in extracellular glucose in the presence of Na^+. Because control cells without Sglt2 transfection showed significant background glucose oscillations due to endogenous transport, conditions were optimized to allow for a greater prominence of specific Sglt2 signal. Oscillations of Na^+/K^+ were superimposed either in conjunction with or in opposition to the glucose oscillations, shifting simultaneously both the co-substrate (Na^+) gradient as well as the transmembrane potential driving Sglt2's electrogenic transport (Figure 3A). Using this paradigm, Sglt2-mediated glucose fluxes (Figures 3B–3D) became distinguishable from transmembrane potential- and Na^+-insensitive background oscillations as intervals of increased amplitude when all gradients favored Sglt2-mediated transport. To ensure that this was Sglt2-specific and not an artifact induced by variations in buffer contents, the Sglt2 inhibitor dapagliflozin (EC_{50} 1.1 nM [Meng et al., 2008]) was added at 500 nM. This quickly and completely abrogated the regions of heightened amplitude, identifying Sglt2 as the cause thereof. Hence, OSTA was shown to work in another system of perhaps more difficult accessibility.

Example 4: EAAT2 Inhibition by TFB-TBOA and Indifference to Salicylate

Due to its prominence and its intricate stoichiometry (3 Na^+, 1 H^+, and 1 glutamate for 1 K^+ [Figure 4A; Levy et al., 1998]), EAAT2

(B) Ratiometric traces from individual cells. Traces are vertically shifted by regular intervals for clarity. Note both abrogation of oscillations as well as pH shift upon exposure to salicylate.

(C) Averaged traces from (B), magnified, with error bars indicating standard deviations. Traces are shifted vertically for clarity.

(D) Absolute values of slopes of traces in (C), with sign of slope represented by color as indicated at left. Traces from control cells are shown in orange and cyan and transfected cells in red and blue. Slopes were calculated from a moving window of seven data points (~3.5 s). Inset bar plot shows relative magnitude of slopes in indicated regions, with control cells omitted for clarity.

(E) Schematic: cells expressing Slc26a2 and loaded with SNARF-5F-AM are perfused with buffers containing 0 and 100 mM SO_4^{2-} ± 10 mM Cl^-, at three different pH values. Signal is the ratio between two emission bands excited with one wavelength (Ex 514 nm, Em 575–595, 595–735 nm; objective EC Plan-Neofluar 10×/0.3 NA M27, imaging rate ~2 Hz; stimulus period 40 s).

(F) Individual traces of pH ratios under oscillating 0–100 SO_4^{2-} derived from 40 transfected and 40 untransfected cells in one field of view, shifted vertically by regular intervals for visualization. pH of solutions is as indicated at top, with 10 mM Cl^- added as indicated.

(G) Averaged traces from (F) magnified, with error bars indicating standard deviations. Traces shifted vertically for clarity.

(H) Absolute values of slopes of traces in (G), with sign of slope represented by color as indicated at left. Traces from control cells are shown in green and maroon and transfected cells in red and blue. Slopes were calculated from a moving window of seven data points (~3.5 s). Inset bar plot shows relative magnitude of slopes in the regions indicated, with control cells omitted for clarity.

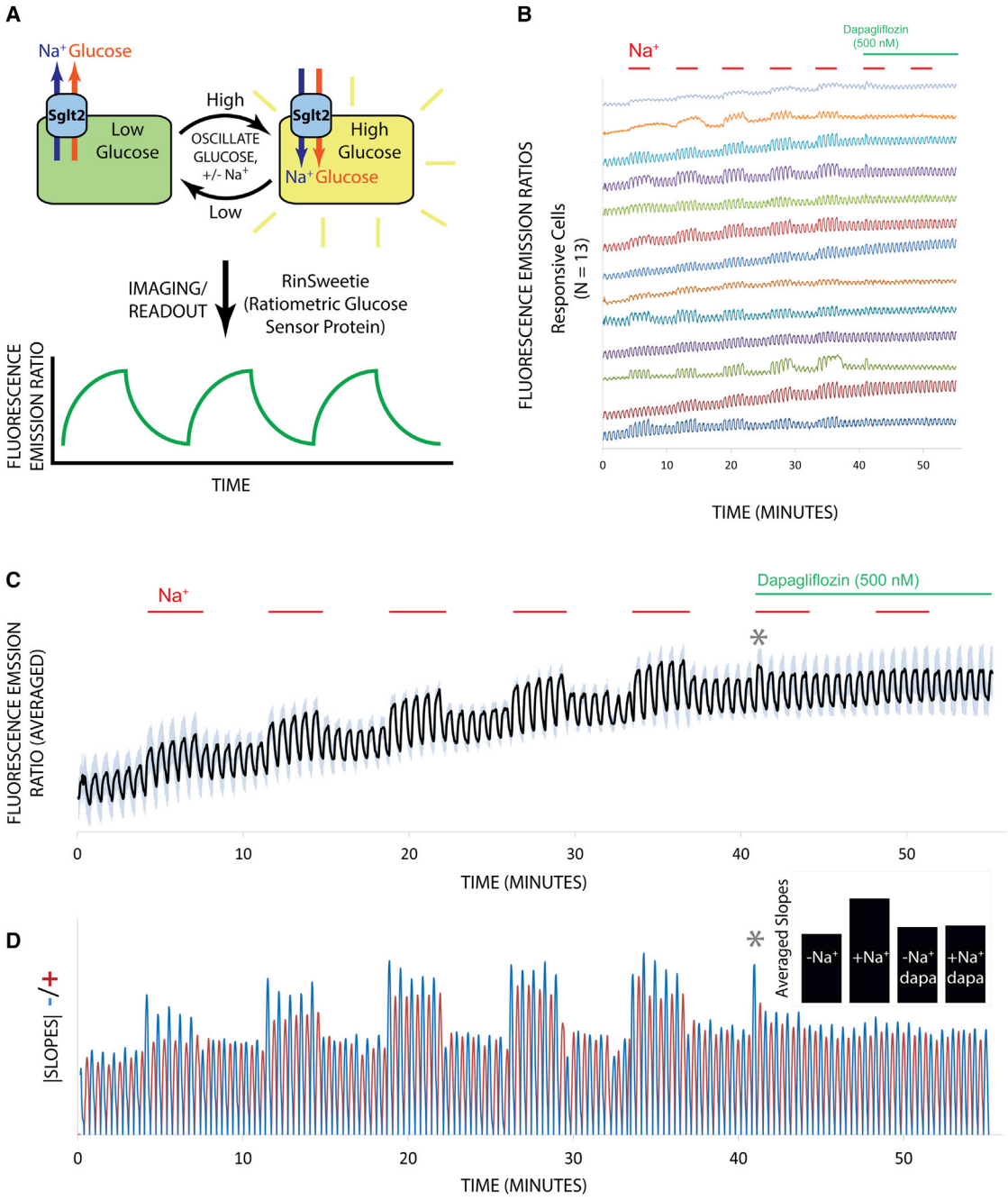

Figure 3. Na^+-Dependent Sglt2-Mediated Glucose Fluxes and Inhibition by Dapagliflozin

(A) Schematic: cells expressing the Na^+-dependent glucose transporter Sglt2 and RinSweetie (an intracellular ratiometric fluorescent glucose sensor protein; J.P.K., A. Simon, J.S. Marvin, J. Shea, H. Lacin, W. Lemon, A. Carruthers, M. Koyama, and L.L.L., unpublished data) are perfused with buffers oscillating between 0 and 2 mM glucose ± 175 mM Na^+. Signal is the ratio between two emission bands excited with one wavelength (Ex 488 nm, Em 505–550, 575–735 nm; objective EC Plan-Neofluar 10×/0.3 NA M27, imaging rate ~2 Hz; stimulus period 40 s).

(B) Individual traces of Na^+/glucose responsive cells. Dapagliflozin, a potent and specific Sglt2 inhibitor, was superadded (500 nM) to perfusion buffers at ~42 min, as indicated. Upward drift is due to photobleaching of red component of ratiometric sensor. Variability of drift is due to variable kinetics of photobleaching observed in the 575–735 nm channel (not shown).

(C) Averaged traces from (B). Asterisk indicates transient response due to dapagliflozin equilibration into perfusion tubing, thereafter promptly squelched by dapagliflozin inhibition. Shading indicates standard deviation between traces after each trace was divided by its time-averaged value.

(D) Absolute values of slopes of response in (C), with polarity indicated by color. Inset: bar plot of responses ± sodium and ± dapagliflozin.

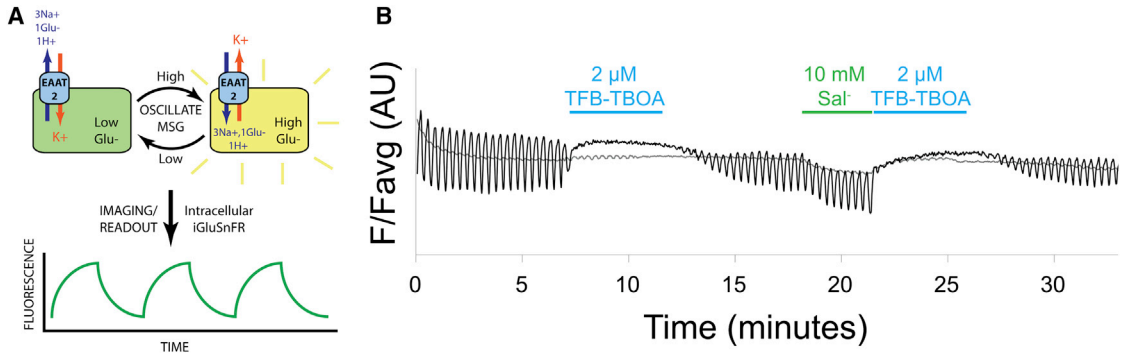

Figure 4. Inhibition of EAAT2 by TFB-TBOA; Indifference to Salicylate

(A) Schematic: cells expressing the Na^+-dependent glutamate transporter EAAT2 and intracellular iGluSnFR (fluorescent glutamate sensor protein [Marvin et al., 2013]) are perfused with buffers oscillating between 0 and 10 mM monosodium glutamate ("MSG"). The signal is emission intensity at one wavelength (Ex 488 nm, Em 505–550; objective EC Plan-Neofluar 10×/0.3 NA M27, imaging rate ~2 Hz; stimulus period 20 s).

(B) Trace of glutamate response in the presence of the EAAT2-specific inhibitor TFB-TBOA (2 μM) and sodium salicylate (10 mM), as indicated. Black trace represents EAAT2-positive response, and gray represents EAAT2-negative. Downward tonic response to salicylate in both traces is likely due to salicylate's known action as a protonophore, which lowers intracellular pH and diminishes iGluSnFR intensity (iGluSnFR has moderate pH sensitivity [Marvin et al., 2013]).

seemed another candidate through which to explore the applicability of the method. The excitatory amino acid transporters (EAATs) were first described in 1978 (Kanner and Sharon, 1978) and have since become well known for their critical role at glutamatergic synapses in the central nervous system (CNS), where they re-uptake the neurotransmitter glutamate and thereby terminate signaling and prevent excitotoxicity (Jensen et al., 2015; Nakagawa and Kaneko, 2013). EAAT2, also known as GLT-1 or SLC1A2, is primarily expressed in astrocytes and is responsible for the majority of glutamate reuptake in the CNS (Tanaka et al., 1997). Defects in EAAT2 are implicated in cerebral stroke, epilepsy, Alzheimer's disease, HIV-associated dementia, Huntington's disease, amyotrophic lateral sclerosis (ALS), and malignant glioma (Shigeri et al., 2004), as well as traumatic brain injury (Yi and Hazell, 2006). EAAT2 is, therefore, a key drug target for these conditions as well as other excitotoxic states.

To evaluate OSTA's efficacy in measuring EAAT-mediated transport, cells were co-transfected with EAAT2 and a cytosolic version of the glutamate sensor iGluSnFR (Marvin et al., 2013), and buffers were oscillated between 0 and 10 mM glutamate; this protocol did not produce significant signals. This was likely due to basal levels of intracellular glutamate saturating the sensor, whose K_d is 80 μM (Marvin et al., 2013). This sensor-saturation hypothesis was corroborated by depriving EAAT2/iGluSnFR-expressing cells of extracellular glutamate overnight: when glutamate was restored, dF/F rose to a maximum of ~2.5 (the maximum when recorded on the surface of HEK cells was ~4 [Marvin et al., 2013]), remained high in the absence of glutamate, and was unresponsive to subsequent glutamate pulses (Figure S1). Hence, it appeared that cells, or at least those used herein, might have a homeostatic mechanism to maintain cytosolic glutamate concentrations above the high micromolar range. The saturation effect might in future experiments be obviated by tuning the sensor to a weaker affinity through targeted mutations to the ligand binding site or the hinge region (Marvin and Hellinga, 2001), some of which have already been described (Marvin et al., 2013). Another potentially confounding aspect of these measurements is EAAT2's co-transport of H^+, which would decrease the sensor's brightness (iGluSnFR is moderately pH sensitive [Marvin et al., 2013]), in opposition to the increases engendered by glutamate. Indeed, several cells showed weak responses of opposite phase to those expected from glutamate, suggesting a H^+-mediated quenching effect on the saturated sensor. Nevertheless, based on pH titrations of the sensor and plausible intracellular pH values, the effect should be small in comparison to larger predicted glutamate-driven oscillations from an unsaturated sensor. These issues are presented to demonstrate potential hurdles in implementation of OSTA; they did not, however, prevent success in any transporter targeted in this study or otherwise.

To overcome the obstacles above, cells were exposed to oscillations of extracellular K^+ (150 mM, Na^+ free) of phase opposite that of Na^+/glutamate. Through this combined Na^+/K^+/glutamate stimulus, EAAT2 was apparently induced to run in reverse and export glutamate, lowering intracellular glutamate levels enough to de-saturate the sensor and unmask a robust oscillating response of appropriate phase in a subset of iGluSnFR-expressing cells. This signal was then harnessed to test the effects of two compounds. Addition of 2 μM of the EAAT2 inhibitor TFB-TBOA completely abolished the oscillations, with rapid onset and slower washout, consistent with its reported high affinity (IC_{50} ~17 nM [Tsukada et al., 2005]). As a negative control, TFB-TBOA was removed and sodium salicylate (10 mM) was added under the same stimulus, with no effect on EAAT2 activity besides a small tonic baseline decrease, probably due to salicylate's activity as a protonophore (Saeedi et al., 2013). An equivalent tonic shift was seen in untransfected cells, indicating that it was EAAT2 independent (Figure 4B). Taken together, these results show that OSTA can be used with a variety of transporters to explore function quickly and easily.

Example 5: Intracellular Organelle Glucose Transport: Endoplasmic Reticulum

Next, experimental conditions were devised to allow measurement of transport in intracellular organelles. There were two main obstacles to attaining this goal: (1) specific localization of the sensor to the organelle of choice, and (2) rapid control of intracellular substrate concentrations. For a test case, glucose transport in the ER was selected, since previous work has already shown glucose fluxes occur in the ER (Fehr et al., 2005), and since an ER-targeted version of the glucose sensor (modified from the sensor used in Example 3; unpublished data) was available in the laboratory. Parenthetically, it should be noted that there are numerous well-characterized protein localization motifs, and this therefore represents a general strategy for targeting protein-based sensors to the organelle of choice, and some similar methods exist for dye-based sensors, e.g., targeting pH indicator dyes to organelles (Benink et al., 2009). The second issue, manipulation of intracellular substrate concentration (glucose in this case), was overcome by screening six different glucose transporters for their rapidity of glucose transport into the cytosol, as measured using OSTA and the cytosolic version of the glucose sensor (~3 hr total imaging). It was determined that Glut1 was by far the fastest under the experimental conditions tested, with some cells exhibiting nearly square-wave responses. Hence, Glut1 expression essentially permeabilized the cell membrane to glucose, enabling oscillating glucose stimuli to reach the ER.

To apply OSTA to ER glucose transport, parallel batches of cells were co-transfected with Glut1 and either the cytosolic or the ER-localized sensor, and OSTA was applied under identical conditions (including solutions, imaging, and processing). Responses were large, fast, and saturating for the cytosolic sensor, but were much smaller, slower, and almost completely linear for the ER-localized sensor (Figure 5). The linearity of the ER transport signal suggests that ER-based transport is rate-limiting and is not complicated by insufficient rapidity in the cytosolic glucose oscillations; this linear signal is therefore a direct and constant temporal readout of glucose transport across the ER membrane. This experiment demonstrates that it is possible, with appropriate experimental design, to use OSTA to measure transporter function even in organelles. It will be of significant interest to determine rates of transport in situ in other types of organelles, in different cell types, under various conditions, or including various pharmacological agents.

Example 6: Temperature and Glucose Transport

Since OSTA uses constant fast perfusion, temperature-controlled experiments can be carried out using temperature-controlled perfusion alone. To test this, the glucose transport of Glut2, as monitored by the cytosolic version of the same glucose sensor as above, was measured at 26°C and 37°C using OSTA. When the perfusate temperature was changed from 26°C to 37°C, an approximately 3-fold change was observed in the magnitude of transport rates (Figure 5D), demonstrating an effect of temperature of roughly the same magnitude as in previous studies, e.g., hexose transport in hepatoma cells changed ~3- to 4.5-fold over this temperature change (Plagemann et al., 1981) or ~3.5- to 4-fold in red blood cells (Hankin and Stein, 1972). This effect was determined not to be an artifact of temperature dependence of the sensor (Figure S2). Although temperature control in the current experiments was achieved simply by running extra lengths of perfusion tubing through a water bath of known temperature, use of a more sophisticated, commercially available temperature-control apparatus would provide means to measure temperature-dependent aspects of transporter function quite readily and precisely, perhaps in conjunction with inhibitors or other experimental manipulations described above, to procure detailed mechanistic information about various transport processes.

Frequency Domain Analysis of OSTA Datasets

In the analysis stage of the above experiments, finding appropriate ROIs (segmentation) was sometimes difficult. One method was to transfect the transporter of interest fused genetically to a fluorescent reporter protein, but this may have perturbed transporter function and, surprisingly, did not provide ideal ROIs. This is due to both weak "lacy" visibility of the reporter due to membrane localization as well as "hot spots" due to non-functional ER-accumulated protein: reporter intensity correlated only poorly with functional signal. Another approach taken was to co-transfect a separate cytosolic reporter protein plasmid, but it was observed that cells often seemed to receive only one of the two plasmids, again leading to poor reporter-function correlation. Upon visual inspection of the image stacks, however, time-dependent oscillating functional signatures were usually quite obvious to the eye. It was realized that these temporal signatures could be computationally identified through Fourier transforms (FTs) of each pixel in the time dimension: pixels with the greatest oscillations would be highlighted in the FT at the stimulus frequency. Since the frequency of the stimulus was known, and the response was presumably of identical frequency, the appropriate images in the Fourier-transformed image stacks (both phase and amplitude) could be selected and used for segmentation of ROIs. This approach is called Fourier Transform OSTA (FT-OSTA).

As a proof-of-principle of this method, data similar to the initial segment of Figure 2 were analyzed. First, pixel-wise temporal fast Fourier transforms (FFTs) of the image stack were computed using a plugin to ImageJ ("stack temporal FFT, jru v1"; http://research.stowers.org/imagejplugins/index.html; see Figure S3 for plugin workflow schematic). This plugin outputs a stack of images with its time domain transformed into frequency domain, with interleaved real and imaginary images; as such, each image represents the real or imaginary response component of all pixels at a given frequency. This stack can be further transformed with separate plugins ("complex amp jru v1" and "complex phase jru v1"; http://research.stowers.org/imagejplugins/index.html) to amplitudes or phases, again with each image representing a particular frequency. For these data, the signal was well isolated in two successive images in the frequency domain stacks (Figures 6A and 6B). These images were then used for the definition of ROIs and measurement of functional data from the original time-domain stack. The functional traces derived from these ROIs displayed much higher signal-to-noise ratios than those derived from other means of segmentation (based on fluorescent co-transfection markers or tagging).

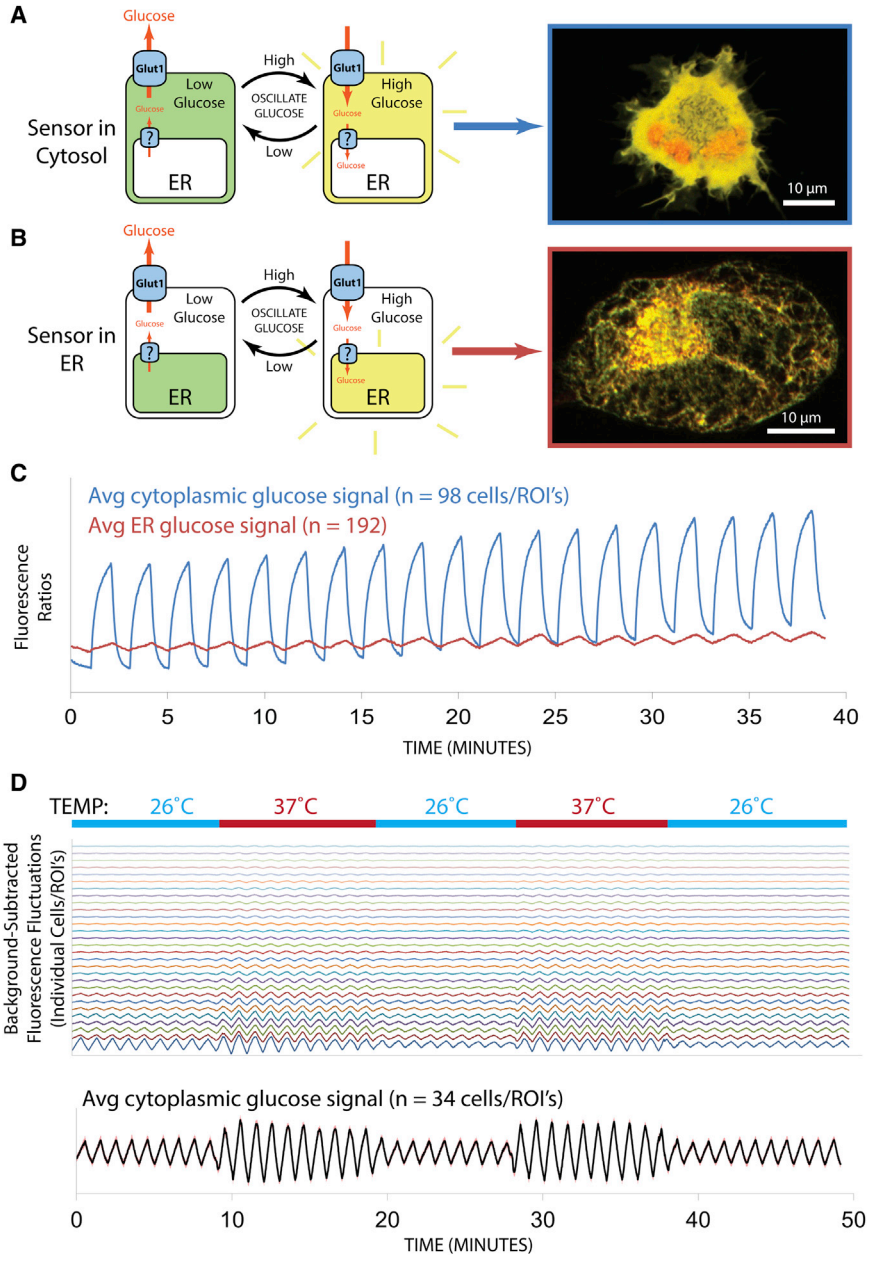

Figure 5. Glucose Transport into ER; Effects of Temperature Changes on Glut2

(A–C) Measurement of relative glucose fluxes into cytosol and endoplasmic reticulum (ER).

(A) Schematic of glucose transport into the cytosol. Sensor is expressed in cytosol and cells are exposed to buffers alternating between 100 mM glucose and sorbitol (inert substitute); the glucose transporter Glut1 was expressed to enhance fluxes. A sample high-magnification image is shown at right (Ex 488/561 nm, Em 495–575/575–617 nm; objective Plan-Apochromat 63×/1.40 NA Oil DIC.)

(B) Schematic diagram of assay for ER glucose. All parameters are the same as in (A), but the sensor in this case is expressed in the ER lumen. A sample high-magnification image is shown at right (same microscopic parameters as in A).

(C) Quantification of glucose fluxes into cytosol and ER (fluorescence ratios of glucose sensor). The ER signal is smaller but still measureable and linear, indicating possibilities for OSTA-based measurement of transport even in subcellular organelles (Ex 488/561 nm, Em 495–575/575–617 nm; objective EC Plan-Neofluar 10×/0.30; stimulus period 120 s.)

(D) Temperature effects on Glut2-mediated glucose transport into cytosol. Top: individual traces of moving-window background-subtracted images are shown, with temperature changes of perfusate shown above. Bottom: average of normalized traces is shown. Note barely visible error bars in red indicating 1 SD. Note also increased amplitude at higher temperature. (Ex 488/561 nm, Em 495–575/575–617 nm; objective EC Plan-Neofluar 10×/0.30; stimulus period 60 s.)

FT-OSTA Analysis in the Presence of Artificial or Experimental Noise

To benchmark FT-OSTA, substantial artificial Gaussian noise (pixel-wise standard deviations increased ~10-fold) was added to the same dataset, and results were compared (Figures 6C–6F). On a visual level, the original images had shown clear cell boundaries and functional signatures, but these disappeared entirely upon addition of noise unless the contrast was carefully adjusted to the original bounds, in which case the cells became barely detectable (Figure 6D). Using only the raw data, definition of ROIs would have been impossible. FT-OSTA analyses were then carried out on both the original and noisy image stacks. A further step was taken this time, however, which was to combine the phase and amplitude information, thus recapitulating a lock-in amplifier and thereby boosting the signal. To establish a metric for signal quantification in the resultant images, a large square ROI was defined over a non-responsive region (outlined in Figure 6D), and its standard deviation was measured for each of the stimulus-frequency FT images. Images were then divided by this standard deviation to provide images calibrated in units of standard deviations (sigma [σ]) above background. The original dataset showed a large signal, with some cells exhibiting signals greater than 50 σ in the amplitude images and greater than 125 σ in the hybrid phase-amplitude images (Figure 6C). As expected, the signal in the noisy dataset was significantly attenuated, but was nevertheless readily detectable, with some cells reaching levels of ~25 σ (Figure 6D). The level of noise in this exercise, as can be seen in one example ROI (Figures 6E and 6F), is probably such to preclude meaningful measurements in the time domain: while a signal's presence is obvious, its quantity is poorly defined without further processing. It is likely, although not

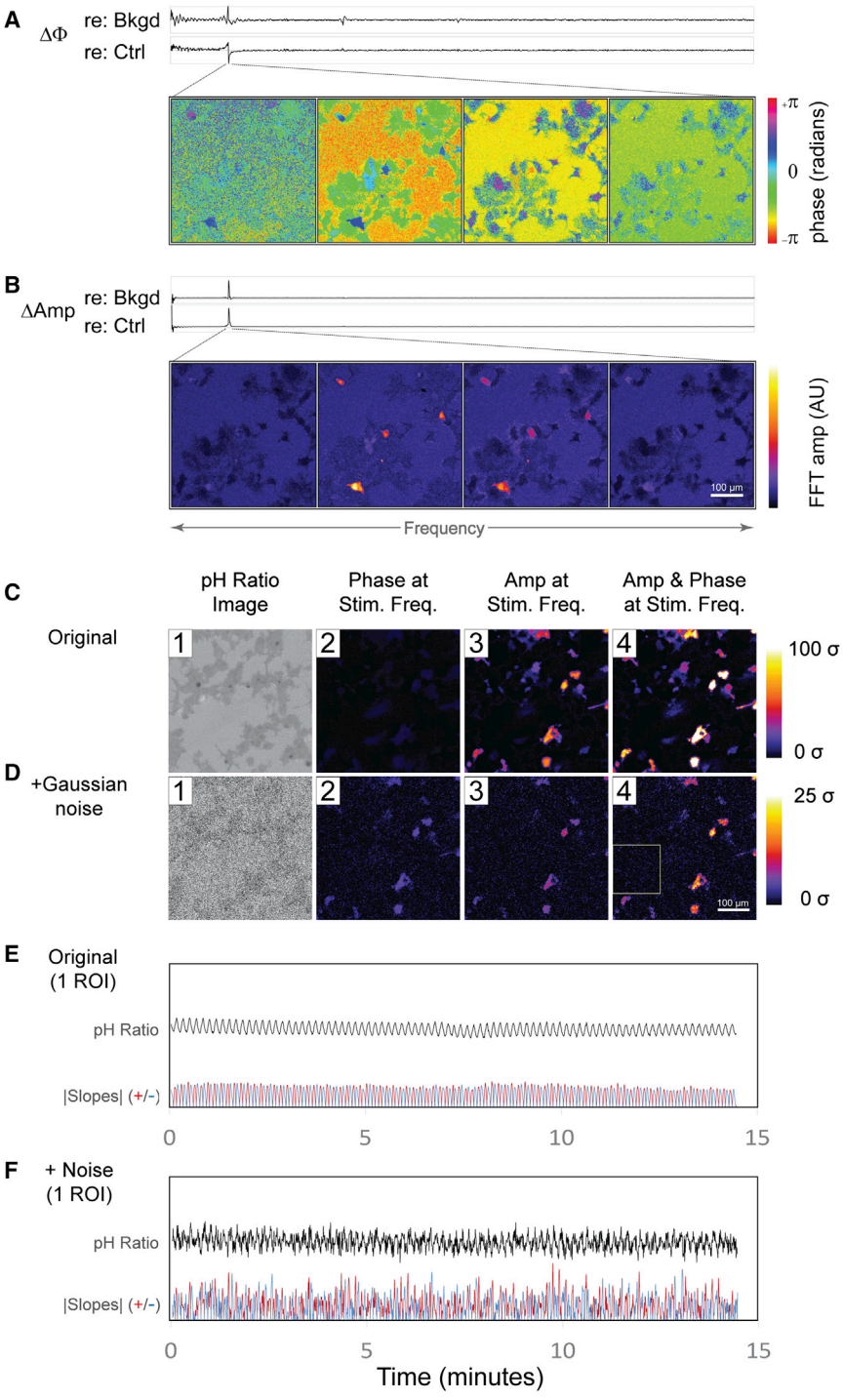

Figure 6. FT Phase and Amplitude versus Frequency in an OSTA Time-Lapse Dataset; Efficacy of Frequency-Domain Analysis in Signal Retrieval from Noisy Datasets

(A) FT phase versus frequency. Top: plots of phase differences between an ROI of a transfected cell versus a non-cell ROI ("Bkgd") or versus a non-transfected cell ROI ("Ctrl"), as a function of frequency. Bottom: images colored by phases at four consecutive frequencies in the transform. Corresponding calculated periods were 20.58, 20.40, 20.22, and 20.05 s (left to right), and experimental stimulus period was set to be 20 s. Source of slight discrepancy is unknown.

(B) FT amplitude versus frequency. Top: plots of amplitude differences between an ROI of a transfected cell versus a non-cell ROI ("Bkgd") or versus a non-transfected cell ROI ("Ctrl"), as a function of frequency. Bottom: images colored by amplitudes at four consecutive frequencies in the transform (periods as in A). Note that amplitude appears to contain more signal than phase under these conditions.

(C1) Example unprocessed image from pH-ratio time-lapse. Cells are distinguishable from background.

(C2) Image of phase differences, at stimulus frequency, relative to a reference transfected cell, colored by standard deviations derived from a background region (scale at far right, background region shown as box in D4; see text for details). Contrast is low to allow for comparison to larger signals in (C3) and (C4).

(C3) Image of amplitudes at stimulus frequency, colored by standard deviations with the same scale as (C2).

(C4) Image of combined phase-difference and amplitude information, colored by standard deviations similarly to (C2) and (C3).

(D1) Example single image from pH ratio time-lapse as in (C1), set to same contrast range as (C1), which tends to enhance visibility of cells. Cells are invisible when contrast range is reset to accommodate all pixel values (not shown).

(D2) Image of phase differences, at stimulus frequency, relative to a reference transfected cell, colored by standard deviations derived from a background region (scale at far right; background region shown as box in D4). Note relative insensitivity of phase information to noise. Note also difference in scale compared to C2–C4.

(D3) Image of amplitudes at stimulus frequency, colored by standard deviations with same scale as (D2).

(D4) Image of combined phase-difference and amplitude information, colored by standard deviations as in (D2) and (D3). Inset rectangle indicates ROI used to compute background standard deviations.

(E and F) Analogous time-domain analysis of one ROI from the same image series, with and without added noise.

(E) Black trace indicates pH ratios from one cell, and the red/blue traces below indicate positive/negative slope magnitudes thereof. Stimulus period 10 s.

(F) Similar to (E) but with the same artificially added noise as in (D1–D4).

explored in the current study, that a combined time-frequency analysis approach via FT analysis of sliding temporal "windows" of images could be used to measure oscillating signals as a function of time, especially with signals of high temporal frequency. (An analogous analysis is in fact done biologically in the auditory system with sounds, where it seems to be highly effective [Gabor, 1946].) In any case, it can be seen from this example that even when the cells themselves become invisible

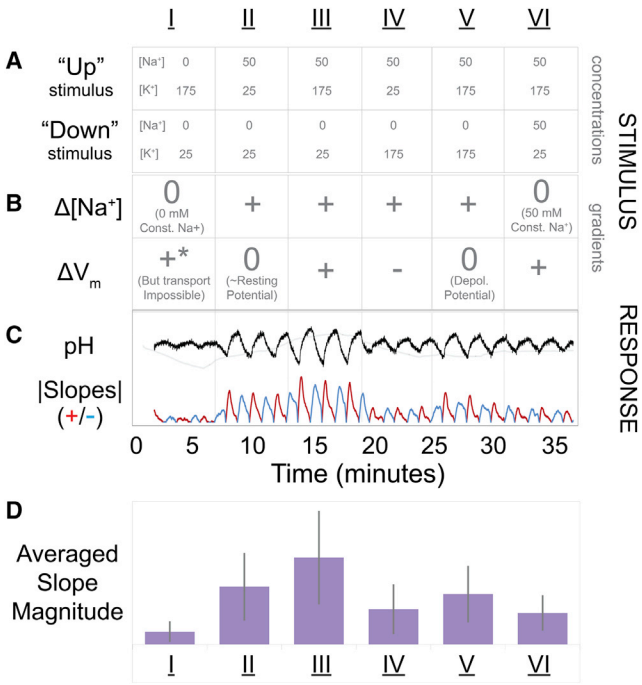

Figure 7. Case Study of FT-Based De-noising: Demonstration of Electrogenicity and Na^+ Dependence of NBC1e-b-Mediated Na^+/HCO_3^- Transport

(A) Concentrations of ions in various stages (stages indicated by roman numerals, top). "Up" and "down" stimulus refer to direction of pH response in (C). Na^+ drives flux directly through co-transport, whereas K^+ affects transport through membrane potential.

(B) Gradients of Na^+ ions or K^+-induced voltage at various stages of experiment. "0" indicates no gradient, and "+" and "−" are arbitrary signs to show whether the gradients promote or oppose transport, based on previously reported transporter properties.

(C) Averaged background-subtracted pH response of FT-identified transfected cells during various stages (black trace) with slope magnitudes thereof shown in red/blue for positive/negative values, respectively. Note magnitudes of changes are greatest when the Na^+ and electrical gradients are in same direction, although either gradient alone is sufficient to drive transport. Gray trace represents subtracted moving-window background (see text). Stimulus period was 120 s.

(D) Bar plots of averaged slope magnitudes during different stages. Error bars represent ± SD.

to conventional microscopy, FT-OSTA methods can reveal signals from responsive cells.

Example 7: FT-OSTA for Testing Electrogenicity and Sodium Dependence of NBCe1-b

To test the method in an actual experimental scenario, a complex and experimentally noisy dataset was re-analyzed using FT-OSTA. Using conventional methods, this dataset appeared to be too noisy to provide definitive information, but by finding the most responsive ROIs through FT-OSTA methods, functional traces were improved enough to allow conclusions to be drawn. The subject of this experiment was the Na^+/HCO_3^- electrogenic cotransporter NBCe1-b, which has a variable stoichiometry of 1 Na^+: 2 or 3 HCO_3^- (Romero et al., 2013). NBCe1-b is critical in renal and ocular physiology, and its mutations have been connected to diseases of these organs (Romero et al., 2013). Since the transporter had previously been found to be electrogenic, altering transmembrane potential by manipulating extracellular K^+ concentrations should augment or diminish transport when in conflict or in concert with Na^+-driven fluxes. Accordingly, permutations of Na^+ and K^+ (Figure 7A) were used to query the transporter for electrogenicity and Na^+ dependence (Figure 7B). Since this transporter responded far more slowly than the others tested in this study, longer periods (120 s) had to be used to achieve measureable signals, and even so, baselines drifted and the response magnitudes were comparatively tiny. Therefore, several image processing techniques were used. First, FT amplitude analyses were carried out on the raw images to find both high-amplitude (transporter-positive) and low-amplitude (control) ROIs. Next, to remove the slowly drifting non-periodic baseline, a moving-window-average subtraction plugin was used ("stack subtract moving average v2"; http://research.stowers.org/imagejplugins/index.html) with a window size matched to the stimulus period. With this arrangement, the plugin subtracts a non-oscillating, smoothly varying baseline (Figure 7C, gray trace), which should not affect the oscillating components. Traces from ROIs were then averaged, and the resultant trace from low-amplitude ROIs was subtracted from that of the high-amplitude ROIs to remove other systematic artifacts. In the end, the FT-OSTA procedures yielded a clean trace (Figure 7C, black trace) that varied under different conditions in ways predicted from the reported stoichiometry, as follows.

In the first stage (I) of the experiment (for this section, refer to Figures 7A–7D), K^+ was oscillated in the absence of Na^+ to change the transmembrane voltage and to confirm NBCe1-b's requirement of Na^+ (Romero et al., 2013). For unknown reasons, relatively small-amplitude oscillations did occur, perhaps because of residual Na^+, or perhaps because Na^+ is not absolutely required. In the second stage of the experiment (II), Na^+ concentrations were oscillated while keeping the K^+ concentration unchanged, resulting in the expected oscillations in pH. In the third stage (III), both oscillating gradients (Na^+- and K^+-driven transmembrane potential) were applied in conjunction, resulting in still larger oscillations in pH. In the next stage (IV), these same oscillations were set in anti-phase, which diminished the oscillations to a magnitude smaller than the single Na^+ gradient, as expected. In the next stage (V), Na^+ oscillations alone were again used to drive transport, but this time at a depolarized potential through increased K^+ concentration. The oscillations did not differ significantly from those at lower K^+ concentrations (stage II), suggesting that tonic transmembrane potential does not affect transporter efficiency through hypothetical voltage-gating or otherwise. Finally, in the last stage (VI), the effects of transmembrane potential oscillations alone were tested and were found to be smaller than Na^+-driven oscillations, but larger than the background oscillations in (I). These findings were in accordance with previously reported results, but were measured in a single experiment testing both Na^+ dependence as well as electrogenicity. It should be noted that the demands of electrogenicity experiments like this one preclude measurements of transporters whose transport cycle involves K^+ ions, e.g., EAAT2, and potentially those involving Cl^-, since cells often

have non-trivial Cl^- conductances, thus confounding the effects of extracellular K^+ on transmembrane potential. In all transporters indifferent to these ions, however, such measurements should be feasible. Although NBCe1-b displayed the weakest response by far of all transporters tested, and might represent a worst-case scenario, nevertheless, the combination of experimental and analytical techniques described above (FT-OSTA) was able to extract data in accordance with previously reported transport properties.

DISCUSSION

The use of fluorescence imaging of sensors driven by an oscillating stimulus (OSTA) has herein been shown to be effective in measuring transporter function for a variety of experimental questions, transporters, and substrates. First, it was shown that salicylate reversibly inhibits the Cl^-/HCO_3^- exchanger Slc26a3, and then the conditions under which the SO_4^{2-}/OH^- exchanger Slc26a2 transports most effectively were shown. Next, inhibition of Sglt2 by dapagliflozin was demonstrated, and EAAT2 insensitivity to salicylate and inhibition by TFB-TBOA were shown. Two other niches, intracellular organelle transport and temperature effects, were then explored. Last, the power of FT-OSTA (akin to lock-in amplifier techniques) was explored for segmentation and functional quantification. Together, these experiments present a compelling rationale for using OSTA methods for transporter functional assays.

Perhaps the essence of the improvement conferred by OSTA is the ability to monitor transporter activity constantly as a function of time. This had not been possible in previous assays because responses were linear for only a small time-fraction of the assay. By oscillating the stimulus in OSTA, a larger fraction of the experimental time is spent in the linear response mode (Figure S4). It is thought, therefore, that further improvements to OSTA will come through continuing this linearity-maximization strategy; several experimental refinements are already available toward this end. First, more sophisticated perfusion systems can provide complete buffer switches in the microsecond regime (e.g., Glasgow and Johnson, 2014) instead of the 1 s switches herein (Figure S5), and use of such a system would eliminate non-linearities associated with buffer changes. Other sources of non-linearity, such as sensor saturation or intracellular substrate accumulation, can be addressed by shortening the period of the oscillations. To do this while retaining sufficient signal, however, will require higher imaging rates than those of the scanning confocal used herein; currently available cameras or spinning disk confocal microscopes will readily provide these increases. At the same time, measureable changes in substrate concentrations will have to occur in the shorter timescales, requiring increased transport rates and/or improved sensors. Transport rates can be increased through optimization of substrate gradients, transporter expression, or even with modest increases in perfusion temperatures. Perhaps the greatest gains, however, will be through improvements in sensor properties. Tailoring the sensor's K_d or improving its brightness and dF/F will translate directly into improved OSTA signals. All of these experimental refinements are currently possible and will present even more opportunities for investigation.

For example, the measurements of EAAT2 described above, if carried out with improved apparatus, could provide detailed information on the kinetics of inhibition by TFB-TBOA or other inhibitors, such as on- and off-rates (k_{on} and k_{off}). This type of information was heretofore accessible through techniques that usually require purified proteins, such as surface plasmon resonance (SPR), and that are especially difficult and artifact-prone in the case of membrane proteins. In contrast, OSTA would provide these measurements on transporters under nearly physiological conditions with little preparation. This type of measurement might be especially advantageous in a high-throughput drug-discovery setting and could drive significant progress in clinically relevant pharmacological modulation of transporter function. Another possibility that might arise with sufficient increases in oscillation frequency would be to implement a moving-window FT approach, using the FT-derived amplitudes and phases to quantify transporter function in hybrid time-frequency space. It is even possible that through FT-OSTA techniques, and with sufficient advances in instrumentation, the activity of single transporter molecules could be visualized and quantified, similar to electrophysiological measurements of single ion channels. The data in the current work, however, are meant to demonstrate that OSTA can be implemented on basic, broadly available equipment and can already provide much valuable information that was previously inaccessible.

LIMITATIONS

In addition to the linearity-limiting parameters mentioned above, other possible confounding elements should be kept in mind when designing experiments. For example, in measuring glucose transport, possible alteration of glucose concentrations by cellular metabolism should be considered. In the current work (Figures 3 and 5), the presence of stable oscillations in the signal as well as specific inhibition of transport seem to demonstrate that transport is the primary basis of the signal. Another caveat is that absolute quantification of substrate concentrations via fluorescent sensors is currently unreliable. The EAAT2/glutamate results herein exemplify this problem, since it was initially difficult to distinguish between transporter inactivity and sensor saturation (see arguments for saturation above). Careful in situ calibration can help to address this issue, but in general this is currently extremely difficult. Many limitations in OSTA are based on the properties of the underlying sensors, and improved sensors will drive further enhancements in OSTA. As discussed above, faster perfusion and improved microscopy will also increase data quality.

EXPERIMENTAL PROCEDURES

Cell Culture

All experiments presented were done on HEK293 (ATCC #CRL-1573) cells transfected using the Amaxa system (Lonza). Cells were cultured after transfection to densities of 50%–90% confluence in 35 mm coverslip-bottomed culture dishes (MatTek), either uncoated or pre-coated with fibronectin (Sigma-Aldrich), and were imaged in situ. Effects of coating on cell adherence were not quantified, but uncoated dishes worked sufficiently well to allow measurements in most cases.

Sensors and Dyes

For pH imaging, 50 μg aliquots of SNARF-5F-AM (ThermoFisher S23923) were dissolved in dimethyl sulfoxide (DMSO) to 20 mM, diluted 1:200 (loading concentration 100 μM) in existing culture medium from dish, and cells were incubated for 20–30 min under time-lapse imaging (1 frame per 10 s) to determine completeness of loading. Cells loaded in this manner provided data for more than 1 hr under constant imaging, and although intensities decayed moderately over time, the ratiometric nature of the dye mostly compensated for decay-related artifacts. For glucose imaging, a cytosolic, ratiometric, genetically encoded glucose sensor (J.P.K., A. Simon, J.S. Marvin, J. Shea, H. Lacin, W. Lemon, A. Carruthers, M. Koyama, and L.L.L., unpublished data) was co-transfected with Sglt2. For glutamate imaging, a version of iGluSnFR (Marvin et al., 2013) was used in which the signal peptide and transmembrane domains were removed, thus targeting the sensor to the cytosol.

Perfusion System

An off-the-shelf, gravity-fed, four-channel perfusion system (VC3-4, ALA Scientific Instruments) was used in all experiments. The bottoms of the 60 ml feeder syringes were raised to a height providing flow rates of 4–8 mL/min depending on the fluid level of the syringes. Buffers were gassed by continuous bubbling with 5% CO_2 when appropriate. For temperature-controlled experiments, an extra length of perfusion tubing (~1 m) was coiled through a water bath of known temperature, with the bath-to-outlet distance (~20 cm) minimized to preserve temperature. The outlet of the system was directed toward the illuminated area of the coverslip dish at a distance of 2–5 mm, and continuous fast suction at the raised edge of the dish removed solutions. The perfusion outlet was Tygon tubing with 1/16" inner diameter (somewhat larger than that in the manifold), which might have slowed the velocity of the buffers, allowing for better cell adhesion. Protocols for buffer switching were carried out by the software provided. Buffer changes were characterized to be > 90% in 1 s and ~100% in 1.5 s (Figure S5).

Imaging System

All imaging was done on an LSM-510 (Zeiss) inverted confocal fluorescence microscope, with excitation at 488, 514, or 561 nm. Objectives were Zeiss EC Plan-Neofluar 10×/0.3 NA M27 and Plan-Apochromat 20×/0.8 NA. Separate experiments not included here indicate that conventional epifluorescence microscopes provide similar results. Imaging was carried out at the fastest frame rate possible (2 Hz) with bi-directional scanning and pixel dimensions of 512 × 512 with either 8- or 16-bit image depth. The lower-magnification objective was preferred due to its inclusion of more cells, and although higher magnification always improved signal-to-noise in individual ROIs, larger numbers of cells were considered preferable for population sampling. Pinholes were set to their maxima, corresponding to z-depths of 126 μm and 25 μm for the 10× and 20× objectives, respectively, to lessen potential motion artifacts in the z dimension. Laser power at 488 and 514 nm was generally set to 100% and nevertheless did not cause noticeable photobleaching, probably because of the fast frame rates, low magnification, and weakness of the aging laser. In the case of the Sglt2 experiment, the 561 nm laser was set to 2%–10% in the attempt to limit photobleaching of the mRuby2 moiety of the glucose sensor, but even at 2% power photobleaching was unavoidable due to a combination of mRuby2's relative photosensitivity as well as its susceptibility to photobleaching from the 488 nm laser used concurrently. The artifact, while noticeable, did not affect conclusions. Detector gains were always set to prevent overloads of pixels.

Construct/Software Availability

The construct for expression of cytoplasmic iGluSnFR in mammalian cells is available from J. Marvin in the Looger lab at Janelia Research Campus. The plasmid encoding EAAT2 was obtained from Addgene (#32814) and that of Sglt2 from the Harvard PlasmID Database (MmCD00315771). The ImageJ plugins used herein were written by Jay Unruh and can be downloaded from http://research.stowers.org/imagejplugins/index.html.

SUPPLEMENTAL INFORMATION

Supplemental Information includes five figures and can be found with this article online at http://dx.doi.org/10.1016/j.molcel.2016.09.001.

AUTHOR CONTRIBUTIONS

J.P.K. conceived of and designed the research, performed all experiments, and analyzed the data. L.L.L. helped analyze data, and both authors wrote the manuscript. Correspondence should be addressed to J.P.K. for methods (jacobpkeller@gmail.com) and to L.L.L. for reagents (loogerl@janelia.hhmi.org).

ACKNOWLEDGMENTS

The authors thank J. Marvin for assistance with iGluSnFR; H. White for cell culture; S. Muallem (NIH/NIDCR) for plasmids encoding Slc26a2, Slc26a3, and NBCe1-b; J. Unruh (Stowers Institute) for coding many of the plugins used herein; Looger lab members, L. Lavis, and H. Lester for valuable discussion; and R. Keller, P. Dallos, and K. Homma for their contributions on the manuscript.

Received: April 27, 2016
Revised: July 18, 2016
Accepted: August 31, 2016
Published: October 6, 2016

REFERENCES

Abdelfattah, A.S., Farhi, S.L., Zhao, Y., Brinks, D., Zou, P., Ruangkittisakul, A., Platisa, J., Pieribone, V.A., Ballanyi, K., Cohen, A.E., and Campbell, R.E. (2016). A bright and fast red fluorescent protein voltage indicator that reports neuronal activity in organotypic brain slices. J. Neurosci. *36*, 2458–2472.

Arosio, D., and Ratto, G.M. (2014). Twenty years of fluorescence imaging of intracellular chloride. Front. Cell. Neurosci. *8*, 258.

Benink, H., McDougall, M., Klaubert, D., and Los, G. (2009). Direct pH measurements by using subcellular targeting of 5(and 6-) carboxyseminaphthorhodafluor in mammalian cells. Biotechniques *47*, 769–774.

Broussard, G.J., Liang, R., and Tian, L. (2014). Monitoring activity in neural circuits with genetically encoded indicators. Front. Mol. Neurosci. *7*, 97.

Canepari, M., and Zecevic, D. (2010). Membrane potential imaging in the nervous system: methods and applications (Springer).

Chaudhuri, B., Hörmann, F., Lalonde, S., Brady, S.M., Orlando, D.A., Benfey, P., and Frommer, W.B. (2008). Protonophore- and pH-insensitive glucose and sucrose accumulation detected by FRET nanosensors in Arabidopsis root tips. Plant J. *56*, 948–962.

Chen, T.W., Wardill, T.J., Sun, Y., Pulver, S.R., Renninger, S.L., Baohan, A., Schreiter, E.R., Kerr, R.A., Orger, M.B., Jayaraman, V., et al. (2013). Ultrasensitive fluorescent proteins for imaging neuronal activity. Nature *499*, 295–300.

Cichon, J., and Gan, W.B. (2015). Branch-specific dendritic Ca(2+) spikes cause persistent synaptic plasticity. Nature *520*, 180–185.

Clarke, R.J., and Khalid, M.A.A. (2015). Pumps, Channels, and Transporters: Methods of Functional Analysis (Wiley).

Dawson, P.A., and Markovich, D. (2005). Pathogenetics of the human SLC26 transporters. Curr. Med. Chem. *12*, 385–396.

Dunlop, J., Bowlby, M., Peri, R., Vasilyev, D., and Arias, R. (2008). High-throughput electrophysiology: an emerging paradigm for ion-channel screening and physiology. Nat. Rev. Drug Discov. *7*, 358–368.

Dwyer, M.A., and Hellinga, H.W. (2004). Periplasmic binding proteins: a versatile superfamily for protein engineering. Curr. Opin. Struct. Biol. *14*, 495–504.

Enterina, J.R., Wu, L., and Campbell, R.E. (2015). Emerging fluorescent protein technologies. Curr. Opin. Chem. Biol. *27*, 10–17.

Fehr, M., Takanaga, H., Ehrhardt, D.W., and Frommer, W.B. (2005). Evidence for high-capacity bidirectional glucose transport across the endoplasmic reticulum membrane by genetically encoded fluorescence resonance energy transfer nanosensors. Mol. Cell. Biol. *25*, 11102–11112.

Gabor, D. (1946). Theory of Communication. Journal of the Institution of Electrical Engineers *93*, 429–457.

Glasgow, N.G., and Johnson, J.W. (2014). Whole-cell patch-clamp analysis of recombinant NMDA receptor pharmacology using brief glutamate applications. Methods Mol. Biol. *1183*, 23–41.

Gong, Y., Huang, C., Li, J.Z., Grewe, B.F., Zhang, Y., Eismann, S., and Schnitzer, M.J. (2015). High-speed recording of neural spikes in awake mice and flies with a fluorescent voltage sensor. Science *350*, 1361–1366.

Grimley, J.S., Li, L., Wang, W., Wen, L., Beese, L.S., Hellinga, H.W., and Augustine, G.J. (2013). Visualization of synaptic inhibition with an optogenetic sensor developed by cell-free protein engineering automation. J. Neurosci. *33*, 16297–16309.

Hankin, B.L., and Stein, W.D. (1972). On the temperature dependence of initial velocities of glucose transport in the human red blood cell. Biochim. Biophys. Acta *288*, 127–136.

Höglund, P., Haila, S., Socha, J., Tomaszewski, L., Saarialho-Kere, U., Karjalainen-Lindsberg, M.L., Airola, K., Holmberg, C., de la Chapelle, A., and Kere, J. (1996). Mutations of the Down-regulated in adenoma (DRA) gene cause congenital chloride diarrhoea. Nat. Genet. *14*, 316–319.

Jensen, A.A., Fahlke, C., Bjørn-Yoshimoto, W.E., and Bunch, L. (2015). Excitatory amino acid transporters: recent insights into molecular mechanisms, novel modes of modulation and new therapeutic possibilities. Curr. Opin. Pharmacol. *20*, 116–123.

Kanner, B.I., and Sharon, I. (1978). Active transport of L-glutamate by membrane vesicles isolated from rat brain. Biochemistry *17*, 3949–3953.

Keller, J., Homma, K., and Dallos, P. (2013). Pixels as ROIs (PAR): a less-biased and statistically powerful approach for gleaning functional information from image stacks. PLoS ONE *8*, e69047.

Ko, S.B.H., Zeng, W., Dorwart, M.R., Luo, X., Kim, K.H., Millen, L., Goto, H., Naruse, S., Soyombo, A., Thomas, P.J., and Muallem, S. (2004). Gating of CFTR by the STAS domain of SLC26 transporters. Nat. Cell Biol. *6*, 343–350.

Lamprecht, G., Baisch, S., Schoenleber, E., and Gregor, M. (2005). Transport properties of the human intestinal anion exchanger DRA (down-regulated in adenoma) in transfected HEK293 cells. Pflugers Arch. *449*, 479–490.

Lamprecht, G., Schaefer, J., Dietz, K., and Gregor, M. (2006). Chloride and bicarbonate have similar affinities to the intestinal anion exchanger DRA (down regulated in adenoma). Pflugers Arch. *452*, 307–315.

Lamprecht, G., Hsieh, C.J., Lissner, S., Nold, L., Heil, A., Gaco, V., Schäfer, J., Turner, J.R., and Gregor, M. (2009). Intestinal anion exchanger down-regulated in adenoma (DRA) is inhibited by intracellular calcium. J. Biol. Chem. *284*, 19744–19753.

Levy, L.M., Warr, O., and Attwell, D. (1998). Stoichiometry of the glial glutamate transporter GLT-1 expressed inducibly in a Chinese hamster ovary cell line selected for low endogenous Na+-dependent glutamate uptake. J. Neurosci. *18*, 9620–9628.

Marvin, J.S., and Hellinga, H.W. (2001). Manipulation of ligand binding affinity by exploitation of conformational coupling. Nat. Struct. Biol. *8*, 795–798.

Marvin, J.S., Schreiter, E.R., Echevarría, I.M., and Looger, L.L. (2011). A genetically encoded, high-signal-to-noise maltose sensor. Proteins *79*, 3025–3036.

Marvin, J.S., Borghuis, B.G., Tian, L., Cichon, J., Harnett, M.T., Akerboom, J., Gordus, A., Renninger, S.L., Chen, T.W., Bargmann, C.I., et al. (2013). An optimized fluorescent probe for visualizing glutamate neurotransmission. Nat. Methods *10*, 162–170.

Meng, W., Ellsworth, B.A., Nirschl, A.A., McCann, P.J., Patel, M., Girotra, R.N., Wu, G., Sher, P.M., Morrison, E.P., Biller, S.A., et al. (2008). Discovery of dapagliflozin: a potent, selective renal sodium-dependent glucose cotransporter 2 (SGLT2) inhibitor for the treatment of type 2 diabetes. J. Med. Chem. *51*, 1145–1149.

Miesenböck, G., De Angelis, D.A., and Rothman, J.E. (1998). Visualizing secretion and synaptic transmission with pH-sensitive green fluorescent proteins. Nature *394*, 192–195.

Miller, A.J. (1995). Ion-selective microelectrodes for measurement of intracellular ion concentrations. Methods Cell Biol. *49*, 275–291.

Musa-Aziz, R., Boron, W.F., and Parker, M.D. (2010). Using fluorometry and ion-sensitive microelectrodes to study the functional expression of heterologously-expressed ion channels and transporters in Xenopus oocytes. Methods *51*, 134–145.

Nakagawa, T., and Kaneko, S. (2013). SLC1 glutamate transporters and diseases: psychiatric diseases and pathological pain. Curr. Mol. Pharmacol. *6*, 66–73.

Ohana, E., Yang, D., Shcheynikov, N., and Muallem, S. (2009). Diverse transport modes by the solute carrier 26 family of anion transporters. J. Physiol. *587*, 2179–2185.

Ohana, E., Shcheynikov, N., Yang, D., So, I., and Muallem, S. (2011). Determinants of coupled transport and uncoupled current by the electrogenic SLC26 transporters. J. Gen. Physiol. *137*, 239–251.

Ohana, E., Shcheynikov, N., Park, M., and Muallem, S. (2012). Solute carrier family 26 member a2 (Slc26a2) protein functions as an electroneutral SOFormula/OH-/Cl- exchanger regulated by extracellular Cl-. J. Biol. Chem. *287*, 5122–5132.

Plagemann, P.G., Wohlhueter, R.M., Erbe, J., and Wilkie, P. (1981). Effect of temperature on kinetics and symmetries of the hexose transporter of Novikoff rat hepatoma cells. Biochemistry *20*, 3366–3370.

Romero, M.F., Chen, A.P., Parker, M.D., and Boron, W.F. (2013). The SLC4 family of bicarbonate (HCO_3^-) transporters. Mol. Aspects Med. *34*, 159–182.

Saeedi, S., Rocher, F., Bonmort, J., Fleurat-Lessard, P., and Roblin, G. (2013). Early membrane events induced by salicylic acid in motor cells of the Mimosa pudica pulvinus. J. Exp. Bot. *64*, 1829–1836.

Sahoo, S., Aurich, M.K., Jonsson, J.J., and Thiele, I. (2014). Membrane transporters in a human genome-scale metabolic knowledgebase and their implications for disease. Front. Physiol. *5*, 91.

Sakmann, B., and Neher, E. (2009). Single-channel recording, Second Edition (Springer).

Santos-Sacchi, J., Song, L., Zheng, J., and Nuttall, A.L. (2006). Control of mammalian cochlear amplification by chloride anions. J. Neurosci. *26*, 3992–3998.

Scalise, M., Pochini, L., Giangregorio, N., Tonazzi, A., and Indiveri, C. (2013). Proteoliposomes as tool for assaying membrane transporter functions and interactions with xenobiotics. Pharmaceutics *5*, 472–497.

Schindelin, J., Arganda-Carreras, I., Frise, E., Kaynig, V., Longair, M., Pietzsch, T., Preibisch, S., Rueden, C., Saalfeld, S., Schmid, B., et al. (2012). Fiji: an open-source platform for biological-image analysis. Nat. Methods *9*, 676–682.

Schneider, C.A., Rasband, W.S., and Eliceiri, K.W. (2012). NIH Image to ImageJ: 25 years of image analysis. Nat. Methods *9*, 671–675.

Shen, Y., Rosendale, M., Campbell, R.E., and Perrais, D. (2014). pHuji, a pH-sensitive red fluorescent protein for imaging of exo- and endocytosis. J. Cell Biol. *207*, 419–432.

Shigeri, Y., Seal, R.P., and Shimamoto, K. (2004). Molecular pharmacology of glutamate transporters, EAATs and VGLUTs. Brain Res. Brain Res. Rev. *45*, 250–265.

Spence, M.T.Z., and Johnson, I.D. (2010). The molecular probes handbook: a guide to fluorescent probes and labeling technologies, Eleventh Edition (Live Technologies Corporation).

Tanaka, K., Watase, K., Manabe, T., Yamada, K., Watanabe, M., Takahashi, K., Iwama, H., Nishikawa, T., Ichihara, N., Kikuchi, T., et al. (1997). Epilepsy and exacerbation of brain injury in mice lacking the glutamate transporter GLT-1. Science *276*, 1699–1702.

Tinberg, C.E., Khare, S.D., Dou, J., Doyle, L., Nelson, J.W., Schena, A., Jankowski, W., Kalodimos, C.G., Johnsson, K., Stoddard, B.L., and Baker, D. (2013). Computational design of ligand-binding proteins with high affinity and selectivity. Nature *501*, 212–216.

Treger, J.S., Priest, M.F., and Bezanilla, F. (2015). Single-molecule fluorimetry and gating currents inspire an improved optical voltage indicator. eLife *4*, e10482.

Tsukada, S., Iino, M., Takayasu, Y., Shimamoto, K., and Ozawa, S. (2005). Effects of a novel glutamate transporter blocker, (2S, 3S)-3-[3-[4-(trifluoromethyl)benzoylamino]benzyloxy]aspartate (TFB-TBOA), on activities of hippocampal neurons. Neuropharmacology *48*, 479–491.

Watanabe, R., Soga, N., Fujita, D., Tabata, K.V., Yamauchi, L., Hyeon Kim, S., Asanuma, D., Kamiya, M., Urano, Y., Suga, H., and Noji, H. (2014). Arrayed lipid bilayer chambers allow single-molecule analysis of membrane transporter activity. Nat. Commun. *5*, 4519.

Woodford, C.R., Frady, E.P., Smith, R.S., Morey, B., Canzi, G., Palida, S.F., Araneda, R.C., Kristan, W.B., Jr., Kubiak, C.P., Miller, E.W., and Tsien, R.Y. (2015). Improved PeT molecules for optically sensing voltage in neurons. J. Am. Chem. Soc. *137*, 1817–1824.

Wright, E.M. (2001). Renal Na(+)-glucose cotransporters. Am. J. Physiol. Renal Physiol. *280*, F10–F18.

Yi, J.H., and Hazell, A.S. (2006). Excitotoxic mechanisms and the role of astrocytic glutamate transporters in traumatic brain injury. Neurochem. Int. *48*, 394–403.

Zhang, J., Campbell, R.E., Ting, A.Y., and Tsien, R.Y. (2002). Creating new fluorescent probes for cell biology. Nat. Rev. Mol. Cell Biol. *3*, 906–918.

Zheng, J., Shen, W., He, D.Z.Z., Long, K.B., Madison, L.D., and Dallos, P. (2000). Prestin is the motor protein of cochlear outer hair cells. Nature *405*, 149–155.